ISSN 0915-633X

NATIONAL INSTITUTE FOR FUSION SCIENCE

Plasma Diagnostics and Atomic Processes

T. Kato

(Received – Dec. 9, 1989)

NIFS-12 Feb. 1990

RESEARCH REPORT
NIFS Series

NAGOYA, JAPAN

Plasma Diagnostics and Atomic Processes

Takako KATO

National Institute for Fusion Science

Nagoya 464-01, Japan

Abstract

Spectroscopic plasma diagnostics with the use of atomic processes are discussed relating to three subjects in the followings.

i) Time resolved X-ray spectra of titanium helium-like ions from tokamaks.
X-ray spectra observed from tokamak plasmas are analysed with a non-ionization equilibrium model which could explain the time behavior of both spectra and ion abundances.

ii) Line intensity ratios of OV ions for temperature and density diagnostics.
Intensity ratios of emission lines from OV ions are calculated for use in temperature and density diagnostics. The line emissions from a tokamak are analysed for the diagnostics of plasma periphery.

iii) Collisional processes in hot dense plasmas.
The collisional ladder-like excitation and ionization in a hot dense plasma are discussed for the dielectronic states. This process enhances the excitation rate coefficients and decreases the resonance contribution to the excitation cross section.

Key words

plasma diagnostics, atomic processes, X-ray spectra, non-ionization equilibrium, VUV spectra, hot dense plasma, excitation rate coefficient

This is a brief summary of my lectures given at several institutes during my stay in USSR in Oct. 1989.

§1. Time resolved X-ray spectra of titanium helium-like ions from Tokamaks

We have analysed time resolved X-ray spectra observed from Tokamak plasmas taking into account the non-ionization equilibrium. Discrepancies between theoretical calculations and measurements for the intensities of the intercombination lines of titanium He-like ions have been found and these phenomena could be explained by taking ion-ion charge exchange processes into consideration. We have constructed a non-ionization equilibrium plasma model which can explain the time behavior of both spectra and ion abundances.

1.1. Plasma diagnostics by spectral lines of He-like ions

We can derive several physical parameters of a plasma from the X-ray spectra of He-like ions. As is well known, the ion temperature can be derived from the doppler width of a resonance line. The electron temperature is obtained from the intensity ratio of dielectronic satellite lines to a resonance line. In Fig.1.1. the energy level diagram for the prominent lines are shown. The lines j and k are pure dielectronic satellite lines. Then the intensity ratios I_k/I_w, I_j/I_w give the values of the electron temperature, where I_k, I_j and I_w indicate the intensities of the satellite lines k and j and the resonance line w, respectively. On the other hand, the line q in Fig.1.1. is produced mainly by the inner-shell excitation of Li-like ions and the line β produced by the inner-shell excitation of Be-like ions. Then the intensity ratios I_q/I_w and I_β/I_w give the ion density ratios n(Li)/n(He) and n(Be)/n(He), respectively, where n(He), n(Li) and n(Be) indicate the ion densities of He-like, Li-like and Be-like ions. The intensities of the intercombination (x and y) and the forbidden (z) lines are affected by the recombination from H-like

ions. Then from the intensity ratios I_x, I_y, I_z/I_w, the ion density ratio n(H)/n(He) can be derived.

The effective rate coefficients to produce the line intensities of w, x, y and z by the excitation from He-like ions and by the recombination from H-like ions including the cascade effects from highly excited states of titanium ions are shown in Fig.1.2[1] by solid lines and dashed lines, respectively. At low temperatures below 1 keV, the effective recombination rates are much higher than the effective excitation rates. The rate coefficients at high temperatures are shown in Fig.1.3. The forbidden line z can be produced by the inner-shell ionization from Li-like ions as shown in Fig.1.1. The rate coefficient to produce the forbidden line by the inner-shell ionization is shown in Fig.1.3 by S_z. The excitation rate coefficients for w of He-like ion and the inner-shell excitation rate coefficients for q from Li-like ions are shown as C_w and C_q, respectively. As the temperature increases, C_w, C_q and S_z increase very rapidly, whereas the other rate coefficients for dielectronic satellite lines such as C_k, and for the forbidden line C_z decrease. C^{eff}_z and α^{eff}_z in Fig.1.3 indicate the effective excitation rate coefficient and the effective recombination rate coefficient for the forbidden line z, respectively.

1.2. X-ray spectra from JIPPT-IIU Tokamak

Time resolved titanium X-ray line spectra from an ohmically heated plasma with neon puffing in JIPP-TII-U Tokamak were measured with a high-resolution crystal spectrometer. We have fitted the observed spectra with synthetic calculations taking all the possible lines into account[1]. From the intensity ratios of the satellite lines to the resonance lines, the electron temperature T_e was obtained every 20 ms. The ion density ratios n(Li)/n(He) and n(Be)/n(He) are also obtained from the spectra every 20 ms.

The results indicate that the plasma is in an ionizing phase at the beginning, reaches nearly an equilibrium at about 80 ms, and then turns into a

recombination phase thereafter following a decrease in the electron temperature. The observed spectra (points) and theoretical synthetic spectra (solid lines) are shown in Fig.1.4.[1] The ion ratios n(Be)/n(He) and n(Li)/n(He) decrease with time until 80 ms. For I_z the contribution of the inner-shell ionization of Li-like ions is found to be important, as shown by hatched regions. This implies that the plasma is ionizing in the initial stage. In the later stage 80-100 ms, the ion ratios increase, thus indicating that the plasma is recombining. In this stage the large discrepancies between the experimental and calculated spectra are found for I_x, I_y and I_z. After 100 ms no appreciable lines were observed.

Since neon gass puffing was performed in this dicharge, we have considered the ion-ion charge exchange process

$$Ti^{21+} + Ne^{z+} \rightarrow Ti^{20+}(nl) + Ne^{(z+1)+} \quad . \qquad (1)$$

Following the calculation by Fujima et al[2], the cross section to $n=5$ has a maximum value and the total rate coefficient for the charge exchange process is 2×10^{-9} cm^3s^{-1} at 1 keV. Assuming that the charge exchange recombination rate to the 4^3F is 3×10^{-11} cm^3s^{-1}, n(H)/n(He)=0.03 and the density of neon ions is 20 % of electron density, we obtain a spectrum which is very similar to the observed spectrum during 80-100 ms as shown in Fig.1.5. If we assume that only 4^3F level is populated by ion-ion charge exchange, the population of 2^3P level is enhanced by radiative transitions, thus producing strong I_x and I_y. The contribution of the charge exchange is shown by hatched regions.

The charge exchange process plays a role also in the time evolution of ion abundances. Generally, the tokamak plasma is not in an ionization equilibrium. We calculate a time evolution of titanium ion abundances, taking into account the variation of the electron temperature as a function of $n_e t^*$ (cm^{-3} s),[1)3)]

$$\frac{dn_z}{dt^*} = S_{z-1}\, n_{z-1}\, n_e + \alpha_{z+1}\, n_{z+1}\, n_e - (S_z + \alpha_z)\, n_z\, n_e \qquad (2)$$

where

$$dt^* = dt(1+t/t_s)^{-1}$$

$$1/t_s = D/(L_T L_N) \quad . \qquad (3)$$

Here, D is the diffusion coefficient and L_T and L_N are the temperature and density scale lengths, respectively. The value t_s is taken to be $\sim 5\times10^{-2}$ s for the diffusion coefficient $D \approx 7500$ cm^{2}s^{-1} to fit well the experimental result. The calculated ion abundances taking into account the varying electron temperature derived from the line intensity ratios are shown in Fig.1.6. It is demonstrated that the ionization process dictates the ion abundances in the ionizing phase until $\sim$ 80 ms and the recombination takes place thereafter. After 80 ms, the charge exchange recombination with neon ions $Ti^{20+} + Ne^{z+} \rightarrow Ti^{19+} + Ne^{(z+1)+}$ becomes important.

$$\frac{dn_z}{dt^*} = S_{z-1} n_{z-1} n_e + \alpha_{z+1} n_{z+1} n_e - (S_z + \alpha_z) n_z n_e \qquad (4)$$

$$+ \sum_i \alpha^{cx}_{z+1} n_{z+1} n^i_{Ne} - \sum_i \alpha^{cx}_z n_z n^i_{Ne}$$

where α^{cx}_{z+1} is the charge exchange recombination rate coefficient for titanium ions of charge $z+1$, n^i_{Ne} is the density of neon ions of charge i. The calculated ion abundances in Fig.1.6 show rapid disappearence of He-like, Li-like and Be-like ions after 90 ms due to the recombination. The ion abundances without charge exchange process are shown by dotted lines, whereas those with charge exchange process are shown by solid lines.

1.3. X-ray spectra from TFTR Tokamak

Time resolved X-ray spectra of He-like ions were measured from TFTR Tokamak[4] as show in Fig.1.7(a). The spectra observed at the initial phase of ohmic heating show that the intensity of w is weaker than those of x, y and z (180-240 ms in Fig.1.7). This suggests that the plasma is recombining, where the effective recombination rate for w is smaller than those for x, y and z at $T_e < 1$ keV

as shown in Fig1.2. In the early phase of discharge, z and q are remarkably strong. Both z and q are produced by inner-shell ionization and inner-shell excitation in Li-like ions, and their rate coefficients are sensitive to the amount of high energy electrons as shown in Fig.1.3 by S_z and C_q. These phenomena imply the contribution of high energy electrons in order to produce H-like ions and z and q lines. We have tried to construct a model which can explain the time evolution of both the ion abundances and the spectra.

We introduce a small fraction of suprathermal electrons. This hot component produces hydrogen like ions. In the interaction region between a hot component and a bulk plasma, the recombination lines can be produced as well as the z and q lines. As explained in Sec.1.1, the electron temperature of bulk plasma is obtained from the intensity ratios of the satellite lines to the resonance line. The ion density ratios n(H) / n(He) and n(Li) / n(He) are also derived from the spectal fits assuming the suprathermal electrons. These values and predicted spectra are shown in Fig.1.7(a). The contributions of high energy electrons are indicated by hatched regions in Fig.1.7(a) and those of recombination are shown in Fig.1.7(b). The derived suprathermal components are 0.03% (7 and 8 keV) for the period of 180 ms-420 ms and 0.1 % (30 keV) for 420-540 ms. The temperatures of the suprathermal electrons are derived from the intensities of the lines q and z.

The calculated ion abundances including the hot component are shown in Fig.1.8 (a) as a function of $n_e t^*$. The ion abundances n(H)/n(He) and n(Li)/n(He) derived from the spectral fits are shown by open circles and open triangles, respectively. Dashed lines indicate the values without a suprathermal component. Fig.1.8(b) shows the ion abundances in a hot component plasma. H-like and He-like ions are produced in the early phase of the plasma.

The ion density ratios n(H)/n(He) and n(Li)/n(He) derived from the spectral fits are plotted as a function of electron temperature of the bulk plasma in Fig.1.9. The values in the ionization equilibrium are plotted by dashed curves. As the electron temperature of the bulk plasma rises with time from 0.45 to 1.53 keV,

the derived ion density ratio n(Li)/n(He) decreases and n(H) /n(He) increases. The value of n(Li)/n(He) is always larger than that in ionization equilibrium. This indicates that the plasma is in an ionizing phase. On the other hand, the derived value of n(H)/n(He) is much higher than that in the ionization equilibrium and increases as the temperature increases. This implies that the plasma is over-ionized and the ionization process still dominates H-like ions. The calculated ion ratios assuming the temperature variation of the bulk plasma are shown by dott-dashed lines, and those including suprathermal electrons are plotted by solid lines.

Although a hot component can account for the time variation of the ion abundance and the spectra, it does not work on the intensities of x and y. The intensity of z must be always larger than x and y with any mixture of n(H), n(He) and n(Li) at any plasma conditions. But the measurements show the spectra that x and y are stronger than z in the period after 420 ms. In order to solve this problem, we consider other processes as follows ;

(1) ion-ion charge exchange

We explained a large excess of x and y in the later phase of the discharge in JIPPT-IIU Tokamak in Sec.1.2. The spectra from TFTR could be explained by the ion-ion charge exchange between titanium ions and oxygen ions ; $Ti^{21+}(1s) + O^{z+} \rightarrow Ti^{20+}(1snl) + O^{z+1}$. Assuming that the effective charge exchange recombination rate is 10^{-11} cm^{-3} s at low temperatures (<1 keV), oxygen contamination required is more than 5% in order that the charge transfer recombination is comparable to the electron recombination. At high temperatures ($\sim$1.5 kev) when the excitation process is effective, the charge exchange recombination rate is comparable to the excitation rate for n(H)/n(He)=0.07 and 10 % of oxygen contamination.

(2) two electron excitation

In order to produce the intercombination lines x and y, two electron excitation following the autoionization can be considered,

$$1s^2 2s + e \rightarrow 1s3dn\ell + e \rightarrow 1s2p + 2e \qquad (2)$$

If the effective rate coefficient of this process is greater than 3×10^{-13} cm^3 s^{-1} at 7 keV and 8×10^{-14} cm^3 s^{-1} at 1.5 keV, the intensities of x and y can be accounted for by this process.

(3) others

Polarization by the suprathermal electrons might affect the intensities x, y, z and w[5]. The line intensities of satellite lines with n=3 and x and y lines may be correlated with each other, because the spectra obtained from Doublet III showed large intensities for n=3 satellite lines comparing to the theoretical calculations.[6]

§2. Line intensity ratios of OV ions for temperature and density diagnostics

2.1. OV ions

Intensity ratios of emission lines from OV ions were calculated for use in temperature and density diagnostics[7]. Fig 2.1. shows the relevant part of the energy level diagram of OV ions. The dashed lines indicate radiative transitions with wavelengths in A.

We used new data based on the R-matrix method including 26 states[8] for the excitation rate coefficients among n=2 and n=3. The proton excitation between fine structure levels of 2s2p ^{3}P and 2p^2 ^{3}P is included. We also include the ionization and recombination processes from/to excited levels to/from next ions which are important in a transient plasma. The inner-subshell ionization from OIV to OV as well as the ionization from metastable states to OVI influence the population of metastable states at $T_e > 100$ eV.

2.2. Line intensity ratios

Be-like OV ions have metastable levels $2s2p\ ^3P_{0,1,2}$ for which the population density is comparable to the ground level for the electron density n_e greater than 10^{12} cm^{-3}. The populations of these levels relative to that of the ground level tend to be constant for $n_e > 10^{13}$ cm^{-3} because of a small value of the transition probability from $2s2p\ ^3P$ to the $2s^2\ ^1S$ ground level. Ionization processes from OV $2s2p\ ^3P$ to OVI 2s or 2p decrease the population of $2s2p\ ^3P$, whereas those from OIV $2s^2 2p$ to OV $2s2p\ ^3P$ and from OIV $2s2p^2$ to OV $2s2p\ ^3P$ increase it. In an ionizing plasma at higher temperatures such as in a Tokamak or a solar flare, this effect becomes important. The population of $2s2p\ ^3P$ relative to $2s^2\ ^1S$ is decreased by about 60 % by the inclusion of the ionization process from OV for $T_e = 100$ eV. Then taking into account the ionization from OIV ions to all the levels of OV ions assuming n(OIV) = n(OV), where n(OIV) represents the density of OIV ions, the relative population of $2s2p\ ^3P$ increases by 50 % for $T_e = 100$ eV. The recombination process is not important for plasmas of $T_e > 5$ eV.

As we have discussed above, the metastable $2s2p\ ^3P$ levels and other triplet levels have varying electron density dependences, and this is utilised for the density diagnostics by the line ratio method. Our calculations including ionization and recombination processes are presented in Fig.2.2. and Fig.2.3. The line intensities for multiplets are summed up for the triplet system. The ratios of lines from levels excited from the same levels are a sensitive function of temperature when the difference in their excitation energies is greater than the electron temperature. In Fig.2.2. the ratios of I(172)/I(630) are shown for $n_e = 10^9$ (solid line), 10^{11} (dashed-dotted line) and 10^{13} cm^{-3} (dashed line) as a function of electron temperature for n(OIV) = 0.0. The dotted line shows the result for $n_e = 10^{13}$ cm^{-3} assuming n(OIV) = n(OV). The contribution of the ionization from OIV ions is negligible in this case (The dashed and the dotted lines nearly coincide). The intensity ratios in the singlet system such as I(220)/I(172) and

I(220)/I(248) exhibit weak small density and temperature dependences as shown in Fig.2.3.(a). The intensity ratios for $T_e = 20$ eV (solid line), 40 eV (dashed dotted line) and 100 eV (dashed line) are shown as a function of the electron density assuming n(OIV) = 0.0. For the case of n(OIV) = n(OV) for $T_e = 100$ eV, the ratios are plotted as dotted lines (The dashed and the dotted lines nearly coincide). Density dependent line ratios involving the triplet system are also shown in Fig.2.3.(b) for I(760)/I(630) and I(1218)/I(630).

2.3. Measurements from JIPPT-IIU Tokamak

The time variations of the line intensities $I_t(172)$, $I_r(630)$ and $I_i(760)$ of OV and $I_r(790)$ of OIV are measured for an ICRF-heated plasma. The plasma is primarily sustained by ohmic heating and is additionally heated by ICRF. The density is rapidly raised by gas puffing just before ICRF heating. The temperature dependent line ratio $I_t(172)/I_r(630)$ and the density dependent line ratio $I_i(760)/I_r(630)$ are plotted in Fig.2.4.(a) and (b), respectively. The derived electron temperature of OV is 150 eV during ohmic heating (60-120 ms), decreases at gas puffing to 60 eV (120 ms) and gradually recovers to 100 eV during the RF pulse (60-200 ms). The electron temperature during ohmic heating is much higher than that expected from an ionization equilibrium to be around 20 eV. This indicates a strong transport of the oxygen ions from the wall towards the plasma center region. We plot the temperature dependent line ratio $I_t(172)/I_r(630)$ for abscissa and the density dependent line ratio $I_i(760)/I_r(630)$ for ordinate in Fig.2.5. by open circles for three phases ; (1) ohmic heating, (2) gas puffing and (3) after RF heating. We can see the variations of the temperature and the density simultaneously on this diagram. From the measured intensity ratio of the reasonance lines of OIV to OV ions, the density ratio n(OIV)/n(OV) is estimated to be about 0.5. Solid lines in Fig.2.5. indicate the calculated values for n(OIV)/n(OV) = 0.5 and dashed lines for n(OIV) = 0 including ionization process. The electron density is derived to be on the order of 10^{12} cm^{-3} for

n(OIV)/n(OV)<0.5. The data point at the first period of ohmic heating indicates the effect of the inner-shell ionization of OIV ions.

§3. Collisional processes in hot dense plasmas

3.1. Enhancement of excitation rate coefficients

It is well known that the ionization rate coefficient is increased by the ladder-like excitation ionization in a hot dense plasma (see Fig.3.1.). We have examined this effect for the dielectronic states of H-like ions.[9] The excitation rate coefficients for 1s → 2s, 2p are found to be increased by this mechanism as well as the ionization rate coefficients.

We consider the dielectronic capture from the H-like ground state $1+e \rightarrow nn'$ (Fig.3.1.). This state autoionizes, $nn' \rightarrow 1+e$, decays radiatively, $nn' \rightarrow nn''+h\nu$ ($n''<n'$), or makes a stabilizing transition, $nn' \rightarrow 1n'+h\nu'$ (Fig.3.1.) at low densities. The last process is dielectronic recombination producing a satellite line. In a dense plasma, however, the collisional process, $nn'+e \rightarrow n(n'+1)+e \rightarrow n(n'+2)+e$, dominates other processes such as autoionization and radiative decay. It may finally be "ionized", $n(n'+m)+e \rightarrow n+2e$. This latter series of processes, dielectronic-capture-ladderlike (DL) excitation-ionization, is the excitation $1+e \rightarrow n+e$ of the H-like ion. The DL excitaion may be understood as the lowering of the threshold energy of the direct excitation to the energy of the critical level.[10] DL excitation and deexcitation rate coefficients for H-like neon ion 1s - 2s and 1s - 2p are shown in Fig.3.2. for a temperature of 10^6 K. When the coupling parameter Γ becomes of the order of unity, our treatment is not valid. In Fig.3.2. the electron density at which $\Gamma=1$ holds is given with the solid arrow.

3.2. Decrease of the resonance contribution to the excitation cross section

The mechanism mentioned in the previous section results in an increase in the excitation rate coefficient of $1s \rightarrow 2\ell$. This increase is well approximated by an extrapolation of the excitation cross section below the thershold energy to a certain energy. However the resonance cross section is decreased by this process at the same time.[11)]

We consider a series of processes of dielectronic capture $1s + e \rightarrow 3pn\ell$ followed by autoionization $3pn\ell \rightarrow 2s + e$ as an example of the reasonance contribution to $1s \rightarrow 2s$ as shown in Fig.3.3. The doubly excited levels 2 sm are grouped into the higher-lying levels and the lower-lying ones ; the critical level between these two groups 2 sm_G (the generalized Griem's critical level[12),13)]) is defined such that the sum of the autoionization probability and the radiative decay probabilities from this level is equal to the total collisional depopulation rate from this level. It can be approximated that the higher-lying levels than 2 sm_G are in a flow of the ladderlike excitation-ionization, which results in $1s \rightarrow 2s$. This corresponds to the lowering of the threshould energy in Fig.3.4. for various electron densities. The dielectronic capture into the higher-lying levels than $3pn_G$, where $3pn_G$ is the generalized Griem's critical level, is lost from the process of autoionization $3pn \rightarrow 2s$ and that the part of the resonance contribution from these levels results in the reduction in the excitation rate coefficient. In Fig.3.4. we give the energy of the critical level ; the principal quantum number n_G for $3pn_G$ is 13.9, 8.3, 5.7, 4.3 and 3.3 for $n_e = 10^{18}$, 10^{19}, 10^{20}, 10^{21} and 10^{22} cm^{-3}, respectively. The disappearance of the resonance cross section $1s \rightarrow 3pn \rightarrow 2s$, corresponds to the extrapolation of the excitation cross section $1s \rightarrow 3p$ to the energy of the critical level $3pn_G$. In Fig.3.4. the cross section for $1s \rightarrow 3p$ is extrapolated below its threshold energy down to the critical energy.

3.3. Extrapolation of resonance cross section below the threshold

The excitaion of a He-like ion $1^1S \rightarrow 2^3S$ is taken as an example. Below the excitaion threshold, the excitation trasnfer $(2^3P)n\ell \rightarrow (2^3S)n'\ell'$ can occur. In a

dense plasma, after dielectronic capture the populations in the $(2^3S)n'\ell'$ are further excited by the ladder-like excitation ionization, and finally "ionized";

$1^1S + e \rightarrow (2^3P)n\ell \rightarrow (2^3S)n'\ell' \rightarrow 2^3S + e$.

Owing to the large excitaion cross section for $1^1S \rightarrow 2^3P$, this process enhances the excitation cross section for $1^1S \rightarrow 2^3S$ substantially. This effect may be expressed as extrapolation of the resonance contribution of the excitation cross section below the excitaion threshold. We have estimated the above effect for OVII excitation rate coefficients and shown them in Fig.3.5.

References

1) T. Kato, S. Morita, K. Masai and S. Hayakawa, Phys. Rev. A 36, 795 (1987)
2) K. Fujima, F. Koike and T. Kato, Annual Review, Institute of Plasma Physics, Nagoya University (1989)
3) K. Masai, Astrophys. Space Sci. 98, 367 (1984)
4) M. Bitter et al. Phys. Rev. A 32, 3011 (1985)
5) M.K. Inal and J. Dubau, J. Phys. B 20, 4221 (1987)
   V.V. Krutov, V.V. Korneev, S.L. Mandelstam, A.S. Shlyaptseva, A.M. Urnov, A.V. Vinogradov and I.A. Zhitnik, Preprint P N Lebedev Physical Institute of the USSR Academy of Sciences, No.133 (1981)
6) T. Kato and K. Masai, Journal de Physique, T 49, C1-349 (1988)
7) T. Kato, J. Lang and K.E. Berrington, A.D.N.D.T. to be published (1990)
8) K.A. Berrington and A.E. Kingston (1989) in preparation
9) T. Fujimoto and T. Kato, Phys. Rev. Lett. 48, 1022 (1982)
10) T. Fujimoto and T. Kato, Phys. Rev. A. 32, 1663 (1985)
11) T. Fujimoto and T. Kato, Phys. Rev. A. 35, 3024 (1987)
12) H.R. Griem, Phys. Rev. 131, 1170 (1963)
13) T. Fujimoto, J. Phys. Soc. Jpn, 47, 273 (1979)
14) A.K. Pradhan, Ap. J. Suppl. 59, 183 (1985)

Figure Captions

Fig.1.1. The energy level diagram of the prominent lines.

Fig.1.2. The effective excitation rate coefficients (solid lines) and the effective recombination rate coefficients (dashed lines) for lines from He-like ions.

Fig.1.3. The rate coefficients at high temperature.
Solid lines are those used in our calculations.[1] Dashed lines for C_z is by Pradhan[14] and S_z is by Bitter et al[4]. Dot-dashed line indicates $\sigma^{rel}_w v$ for the resonance line by high energy electrons including relativistic effect.

Fig.1.4. The observed (points) and the theoretical (solid lines) spectra obtained from an ohmically heated plasma of JIPPT-IIU discharge with neon puffing.

Fig.1.5. A calculated spectra taking into account the ion-ion charge exchange process (1) to simulate the observed spectrum in Fig.1.4. (80-100 ms). Hatched regions indicate the contributions of the charge exchange process.

Fig.1.6. Ion abundances for Ti ions vs. $n_e t^*$ including the ion-ion charge exchange are shown by solid lines. The electron temperature is shown by a dashed line. The dotted lines show the results without the ion-ion charge exchange process. The experimental ion abundances normalized to that of He-like ions are compared.

Fig.1.7. Observed (dots) and calculated (solid lines) spectra in 60 ms intervals from an ohmically heated plasma of TFTR discharge.
(a) Hatched regions represent the contribution of a hot component through excitation, inner-shell excitation and inner-shell ionization.

(b) Hatched regions indicate the contribution of the recombination from H-like ions.

Fig.1.8.(a) The calculated ion abundances for titanium ions against $n_e t^*$ including hot component (solid lines). The dashed lines show the ion abundances assuming only the temperature variation of a bulk plasma. The derived ion abundances from the spectra normalized to that of the He-like ions are compared.

(b) The calculated ion abundances in a hot component plasma.

Fig.1.9. Ion density ratios of n(Li)/n(He) and n(H)/n(He) against the electron temperatures. Dashed lines are the calculated values in the ionization equilibrium. Dott-dashed lines indicate the time dependent ratios assuming the temperature variation of a bulk plasma. Solid lines are those including a hot component.

Fig.2.1. Schematic energy level diagram of OV ions.

Fig.2.2. Temperature sensitive line intensity ratios I(172)/I(630).

Fig.2.3.(a) Line intensity ratio I(220)/I(170) in the singlet system as a function of the electron density.

(b) Density sensitive line intensity ratios I(760)/I(630) and I(1218)/I(630).

Fig.2.4. Time behaviors of line intensity ratios (a) $I_t(172)/I_r(630)$ and (b) $I_i(760)/I_r(630)$ of OV ions measured from JIPPT-IIU Tokamak.

Fig.2.5. Plot diagram for $I_t(172)/I_r(630)$ and $I_i(760)/I_r(630)$. Solid lines indicate the calculated values for n(OIV)/n(OV) = 0.5 and dashed lines for n(OIV) = 0.

Fig.3.1. Schematic energy level diagram of H-like and He-like ions. Transitions due to electronic collisions are denoted with solid arrows, radiative transitions with wavy arrows, and autoionization with a dotted arrow, respectively.

Fig.3.2. DL excitation and deexcitation rate coefficients for H-like neon-ion transition 1s - 2s and 1s - 2p. Dashed arrow shows n_e at which the lowering of the ionization potential reaches to $n'=2$ level and the solid arrow shows n_e at $\Gamma=1$.

Fig.3.3. Schematic energy level diagram showing the dominant atomic process for the doubly excited ions in the plasma.

Fig.3.4. The reasonance contributions from the doubly excited levels to the excitation cross section 1s$\rightarrow$2s of H-like neon ions. The energy of the critical level is indicated with the thick lines, and the part of the resonance cross section at higher energies than the critical energy disappears.

Fig.3.5. The excitation rate coefficients taking into account the effect in Sec.3.2. ($1^1S \rightarrow 2^3P$) and Sec.3.3. ($1^1S \rightarrow 2^3S$) for OVII ions at $T_e=2\times10^6$ K in hot dense plasma.

Fig.1.1.

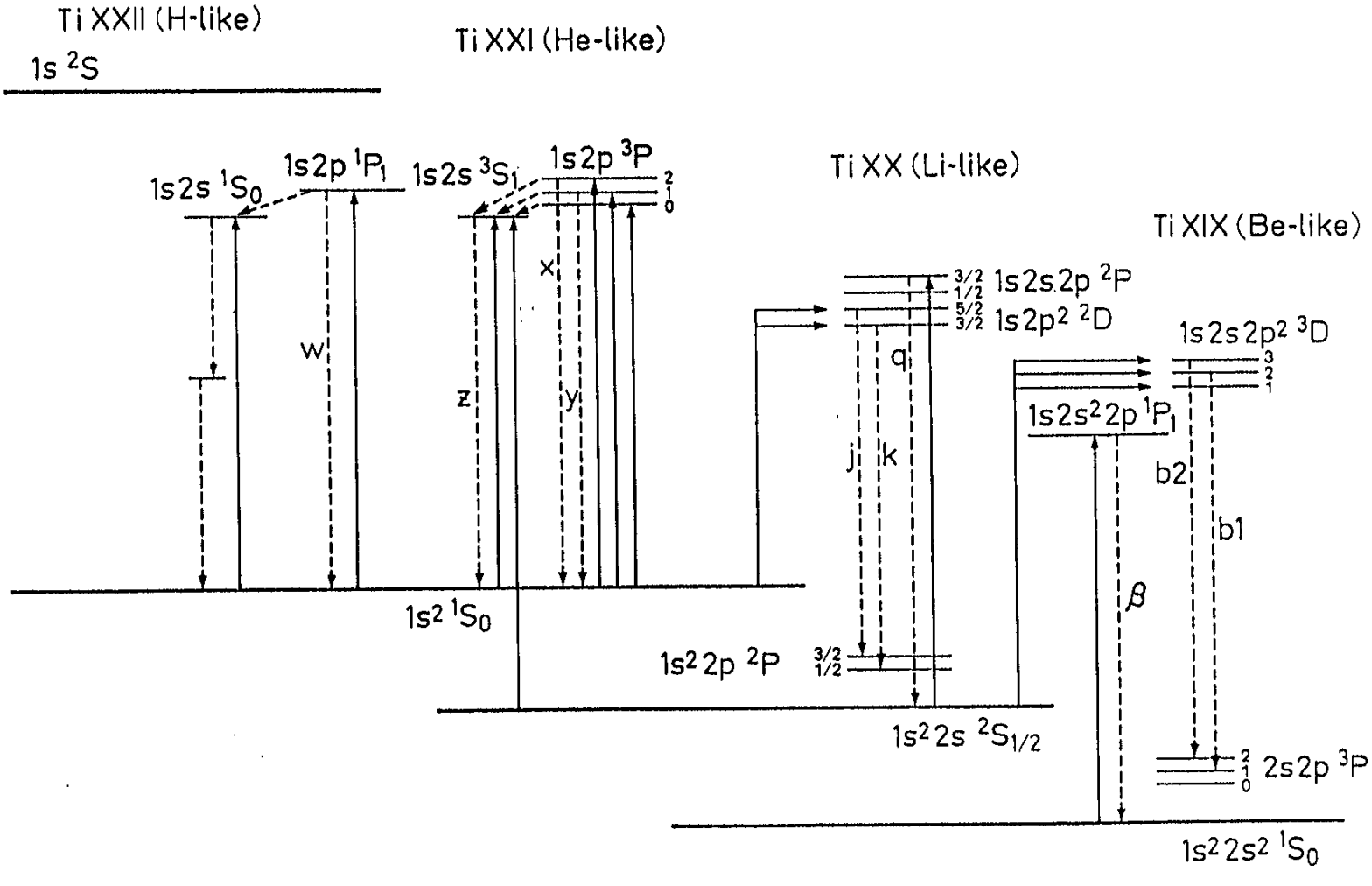
Ti XXII (H-like)
1s ²S
Ti XXI (He-like)
1s2s ¹S₀
1s2p ¹P₁
1s2s ³S₁
1s2p ³P
2
1
0
Ti XX (Li-like)
Ti XIX (Be-like)
w
x
z
y
3/2
1/2
5/2
3/2
1s2s2p ²P
1s2p² ²D
1s2s2p² ³D
3
2
1
q
j
k
1s2s²2p ¹P₁
b2
b1
β
1s² ¹S₀
1s²2p ²P
3/2
1/2
1s²2s ²S₁/₂
2
1
0
2s2p ³P
1s²2s² ¹S₀

Fig.1.2.

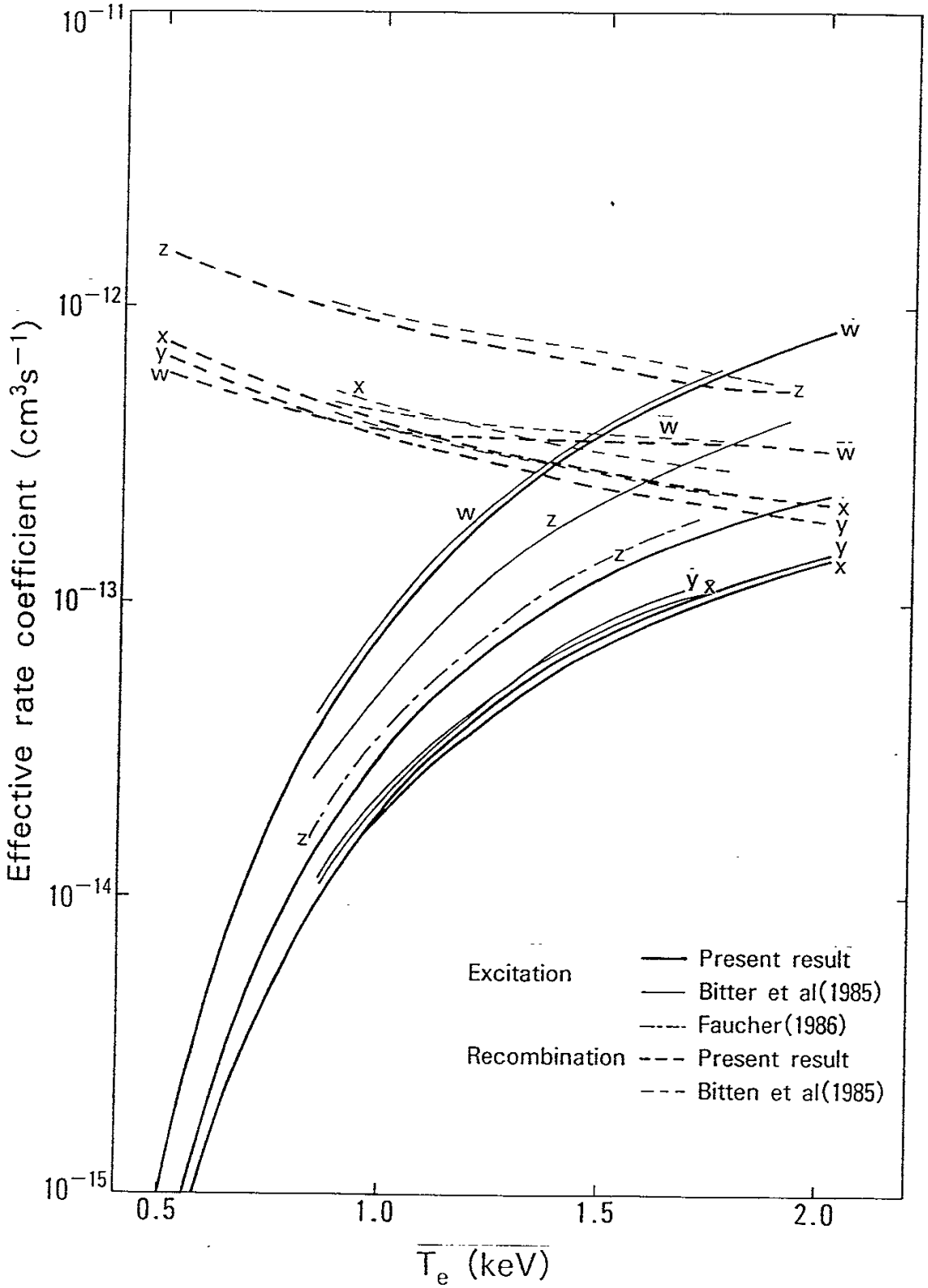
Effective rate coefficient (cm^{3}s^{-1})
10^{-11}
10^{-12}
10^{-13}
10^{-14}
10^{-15}
0.5
1.0
1.5
2.0
$\overline{T_e}$ (keV)
z
x
y
w
x̄
w̄
Excitation
Present result
Bitter et al(1985)
Faucher(1986)
Recombination
Present result
Bitten et al(1985)

Fig.1.3.

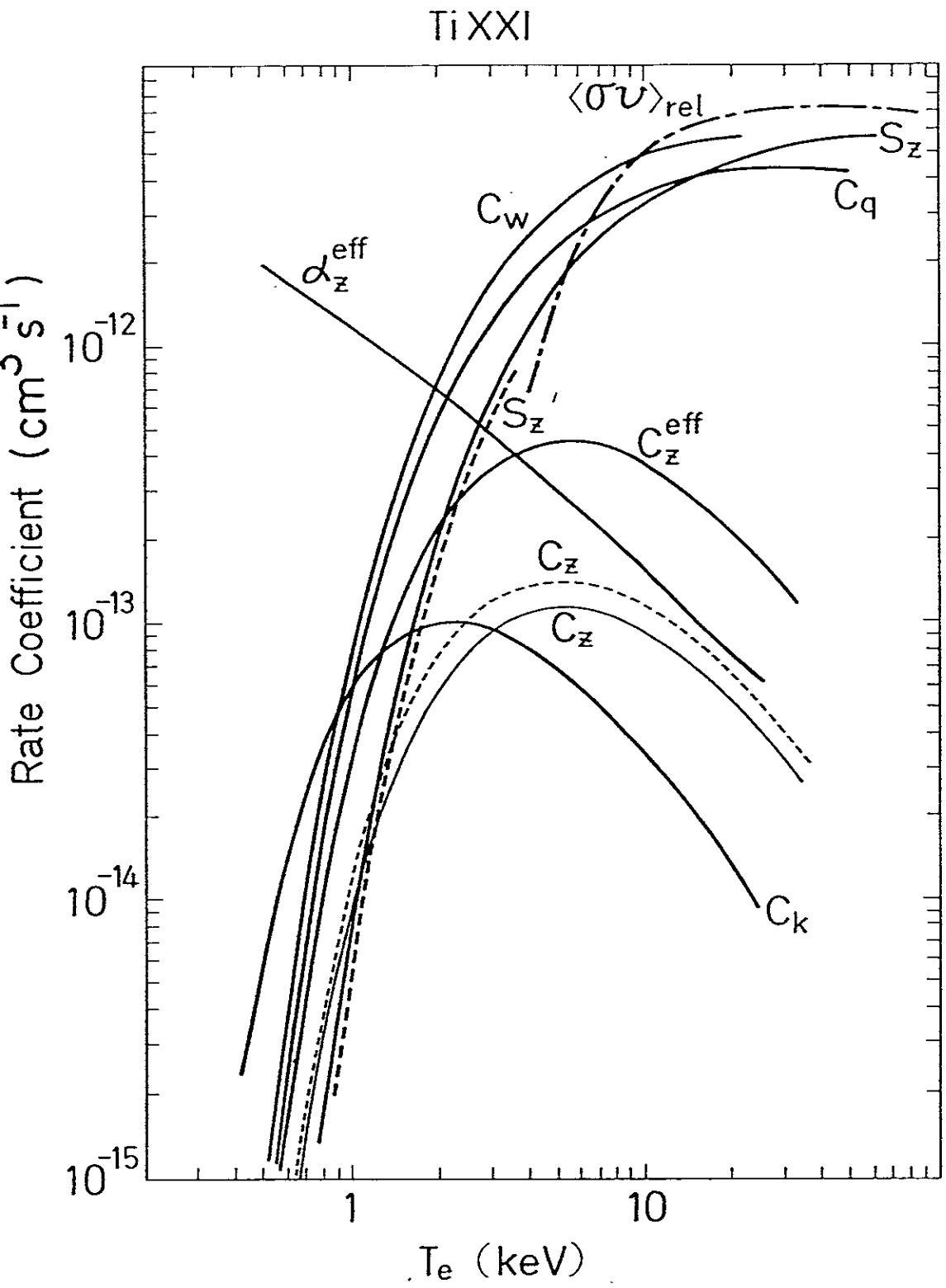
Ti XXI
$\langle\sigma v\rangle_{rel}$
S_z
C_q
C_w
α_z^{eff}
S_z'
C_z^{eff}
C_z
C_z
C_k
Rate Coefficient ($cm^3 s^{-1}$)
10^{-12}
10^{-13}
10^{-14}
10^{-15}
1
10
T_e (keV)

Fig.1.4.

(a)

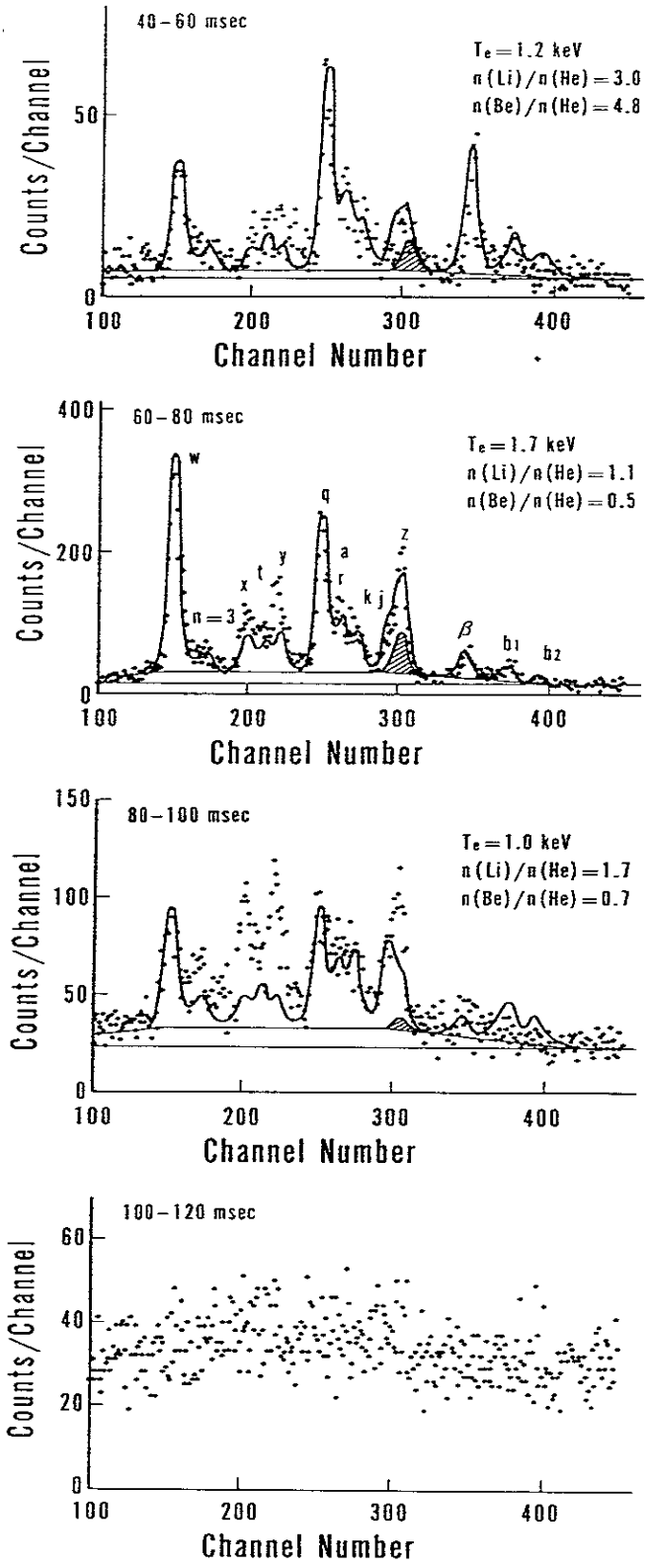
40–60 msec
$T_e = 1.2$ keV
n(Li)/n(He) = 3.0
n(Be)/n(He) = 4.8
Counts/Channel
Channel Number
60–80 msec
$T_e = 1.7$ keV
n(Li)/n(He) = 1.1
n(Be)/n(He) = 0.5
w
q
z
a
r
y
t
x
k j
n = 3
β
b1
b2
80–100 msec
$T_e = 1.0$ keV
n(Li)/n(He) = 1.7
n(Be)/n(He) = 0.7
100–120 msec

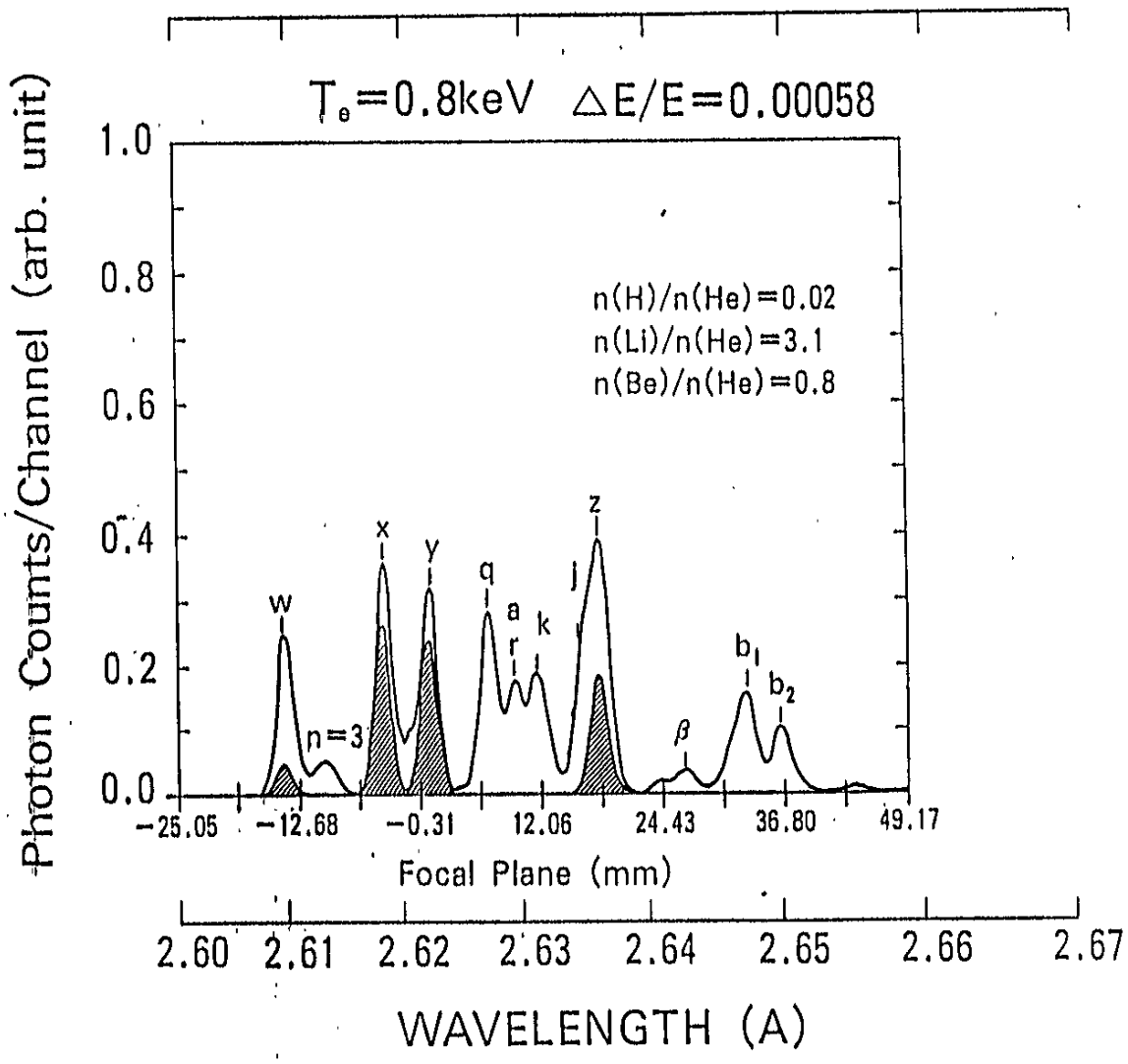
T_e=0.8keV △E/E=0.00058
n(H)/n(He)=0.02
n(Li)/n(He)=3.1
n(Be)/n(He)=0.8
Photon Counts/Channel (arb. unit)
1.0
0.8
0.6
0.4
0.2
0.0
w
n=3
x
y
q
a
r
k
j
z
β
b_1
b_2
−25.05
−12.68
−0.31
12.06
24.43
36.80
49.17
Focal Plane (mm)
2.60
2.61
2.62
2.63
2.64
2.65
2.66
2.67
WAVELENGTH (A)

Fig.1.5.

Fig.1.6.

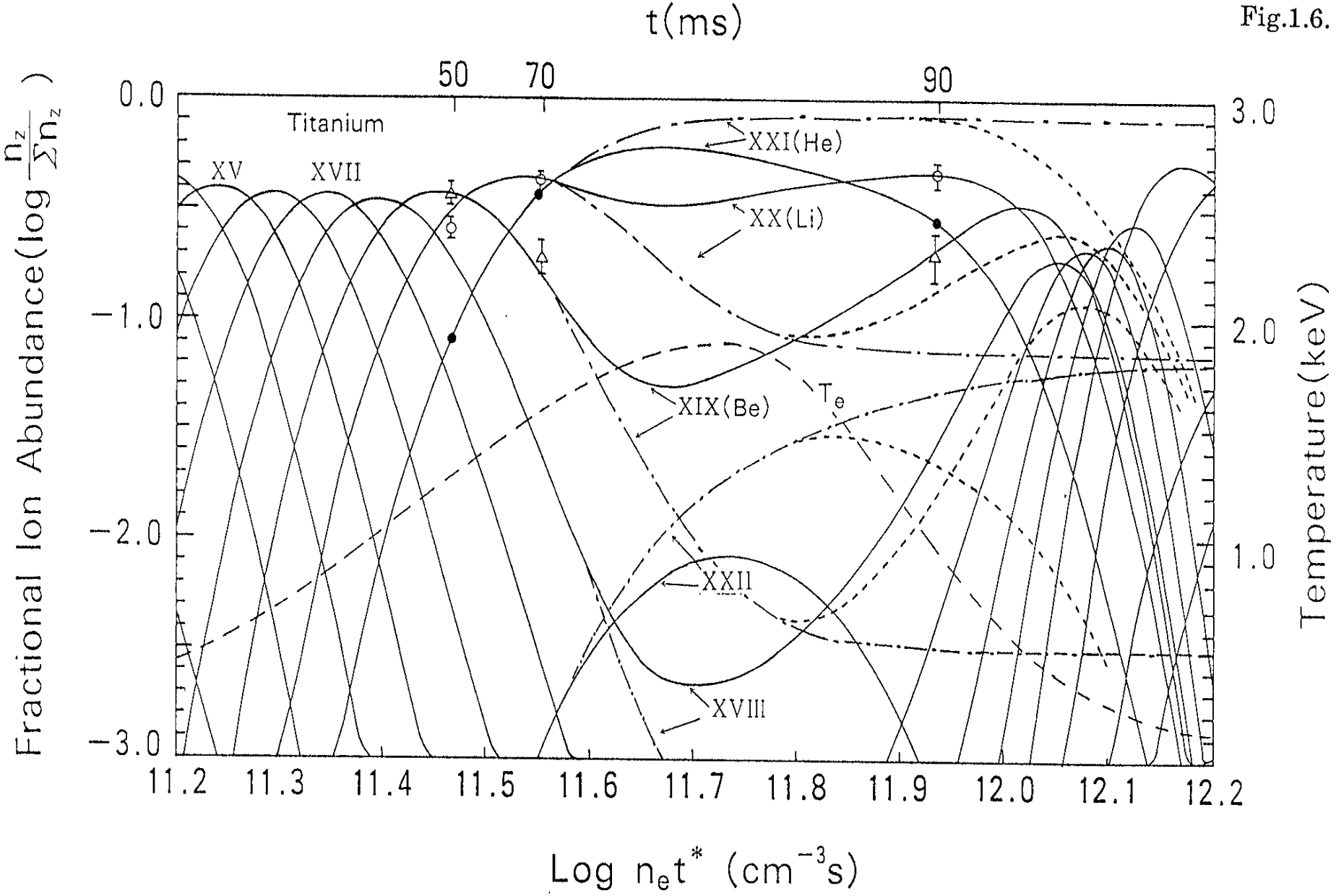
t(ms)
50
70
90
Titanium
XV
XVII
XXI(He)
XX(Li)
XIX(Be)
T_e
XXII
XVIII
0.0
−1.0
−2.0
−3.0
3.0
2.0
1.0
11.2
11.3
11.4
11.5
11.6
11.7
11.8
11.9
12.0
12.1
12.2
Fractional Ion Abundance(log $\frac{n_z}{\sum n_z}$)
Temperature(keV)
Log $n_e t^*$ ($cm^{-3}s$)

Fig.1.7.(a)

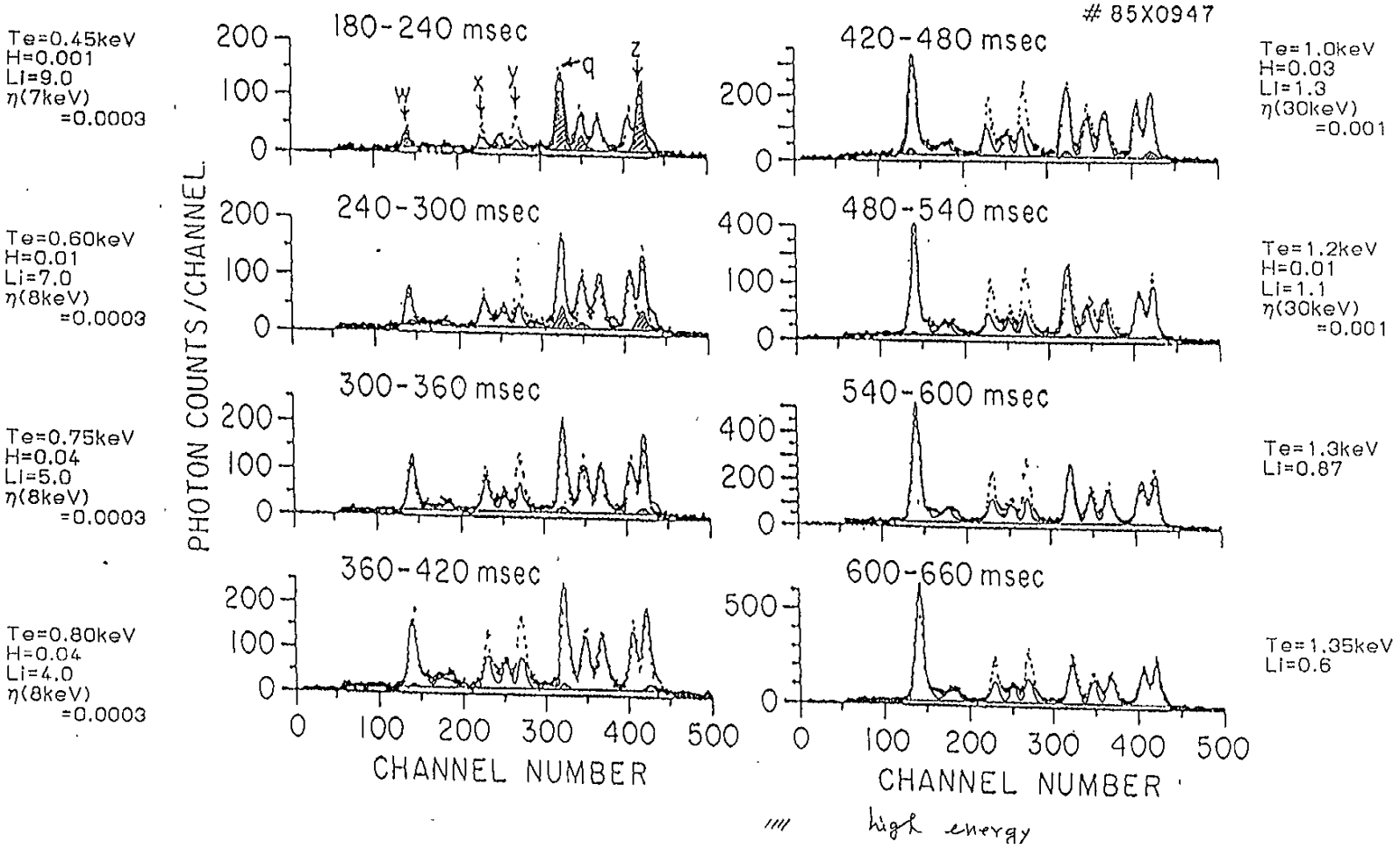
#85X0947
180-240 msec
240-300 msec
300-360 msec
360-420 msec
420-480 msec
480-540 msec
540-600 msec
600-660 msec
W
X
Y
q
Z
PHOTON COUNTS/CHANNEL
CHANNEL NUMBER
CHANNEL NUMBER
Te=0.45keV
H=0.001
Li=9.0
η(7keV)
=0.0003
Te=0.60keV
H=0.01
Li=7.0
η(8keV)
=0.0003
Te=0.75keV
H=0.04
Li=5.0
η(8keV)
=0.0003
Te=0.80keV
H=0.04
Li=4.0
η(8keV)
=0.0003
Te=1.0keV
H=0.03
Li=1.3
η(30keV)
=0.001
Te=1.2keV
H=0.01
Li=1.1
η(30keV)
=0.001
Te=1.3keV
Li=0.87
Te=1.35keV
Li=0.6
//// high energy

Fig.1.7.(b)

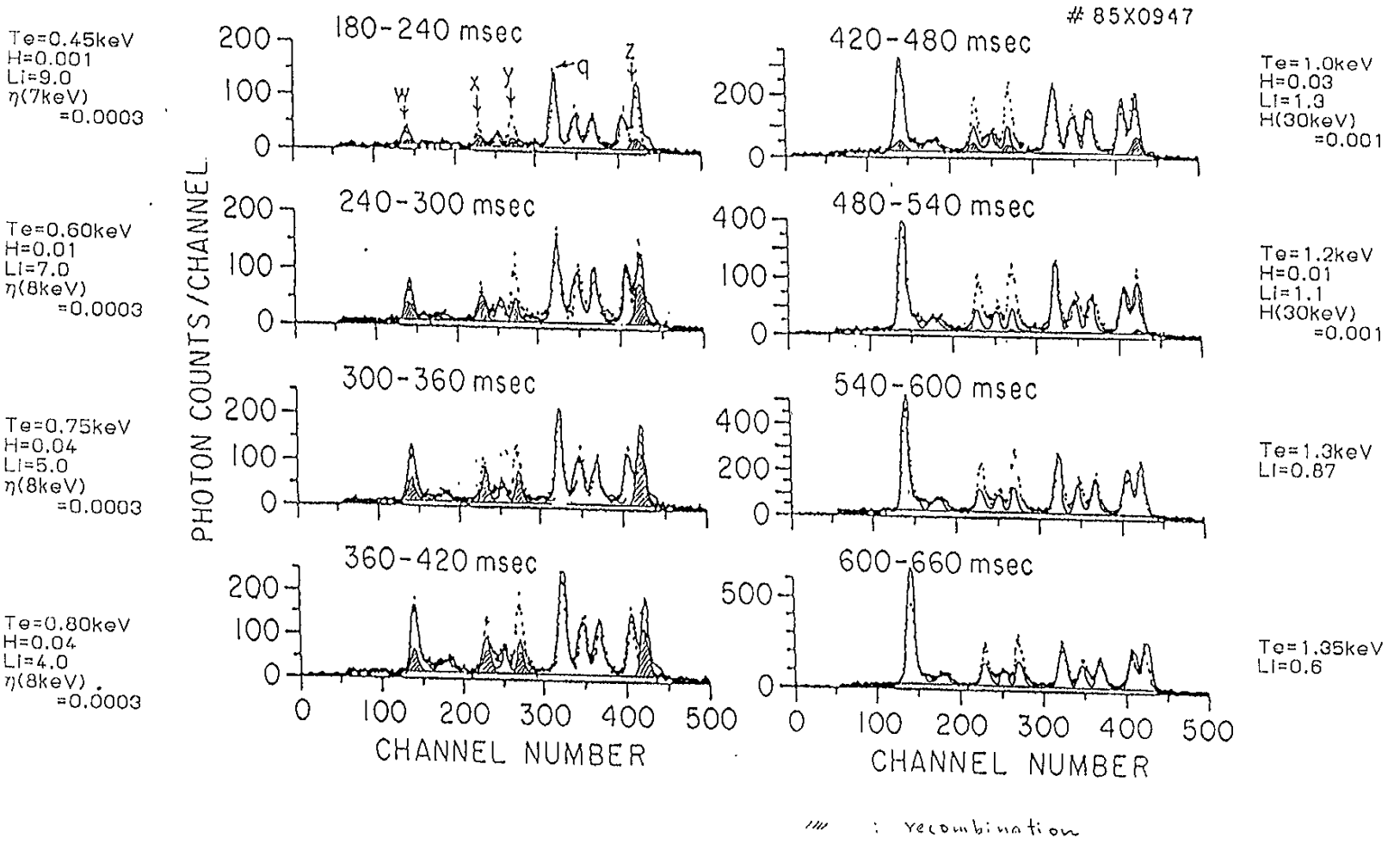
85X0947
180-240 msec
240-300 msec
300-360 msec
360-420 msec
420-480 msec
480-540 msec
540-600 msec
600-660 msec
W
X
Y
q
Z
PHOTON COUNTS/CHANNEL
CHANNEL NUMBER
CHANNEL NUMBER
Te=0.45keV
H=0.001
Li=9.0
η(7keV)
=0.0003
Te=0.60keV
H=0.01
Li=7.0
η(8keV)
=0.0003
Te=0.75keV
H=0.04
Li=5.0
η(8keV)
=0.0003
Te=0.80keV
H=0.04
Li=4.0
η(8keV)
=0.0003
Te=1.0keV
H=0.03
Li=1.3
H(30keV)
=0.001
Te=1.2keV
H=0.01
Li=1.1
H(30keV)
=0.001
Te=1.3keV
Li=0.87
Te=1.35keV
Li=0.6
/// : recombination

Fig.1.8.(a)

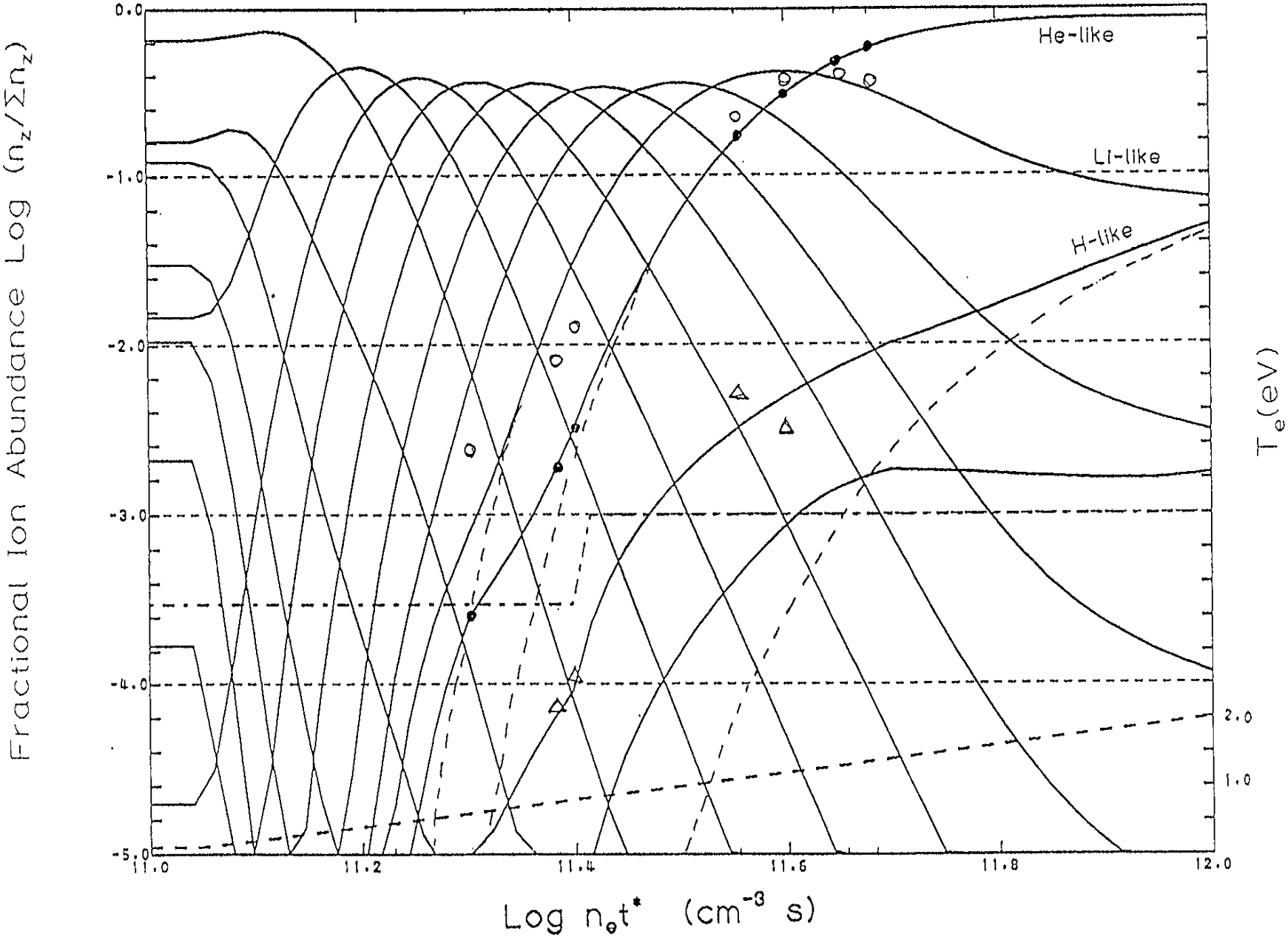
Fractional Ion Abundance Log ($n_z/\Sigma n_z$)
0.0
-1.0
-2.0
-3.0
-4.0
-5.0
He-like
Li-like
H-like
T_e(eV)
2.0
1.0
11.0
11.2
11.4
11.6
11.8
12.0
Log $n_e t^*$ (cm^{-3} s)

Fig.1.8.(b)

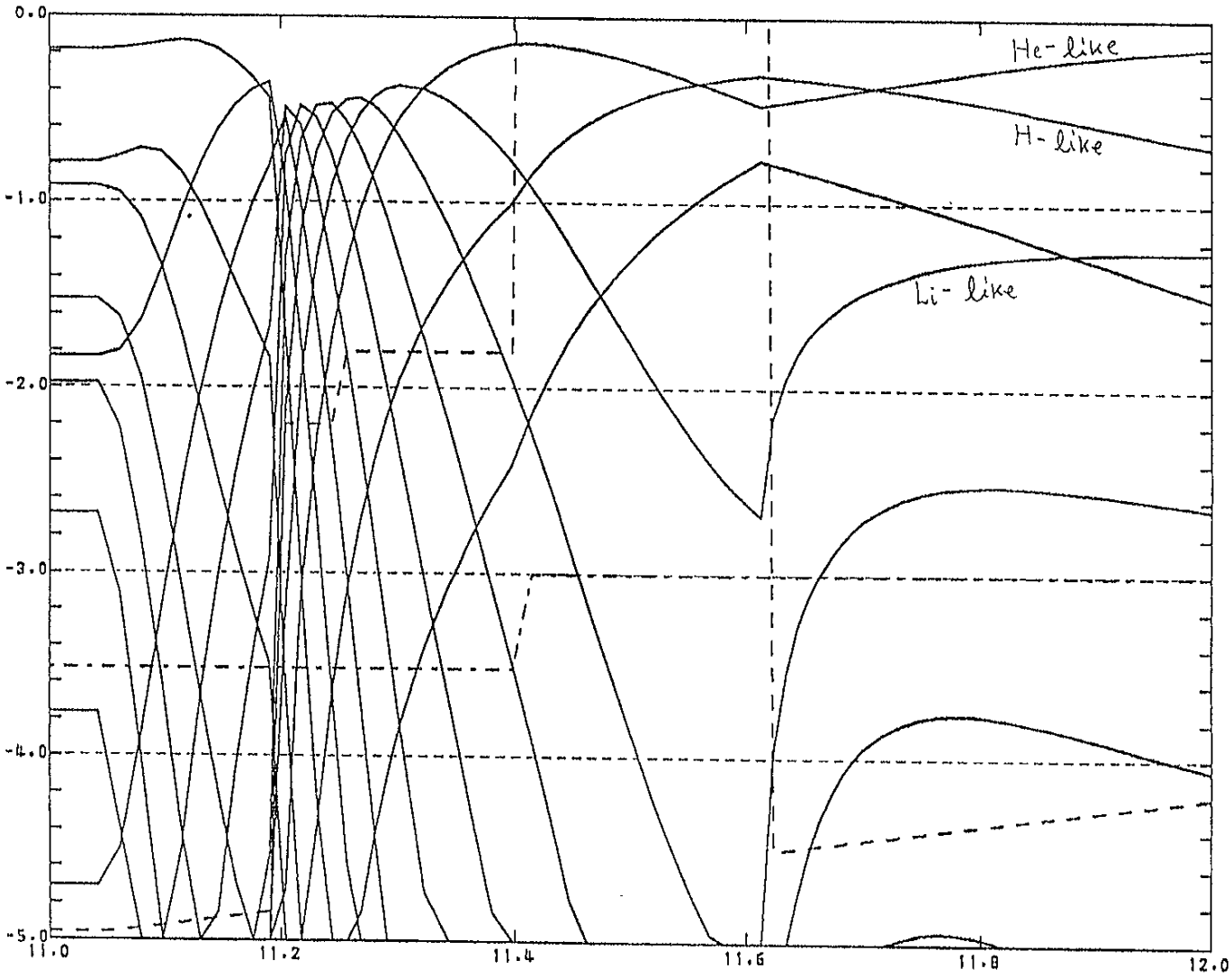

Fig.1.9.

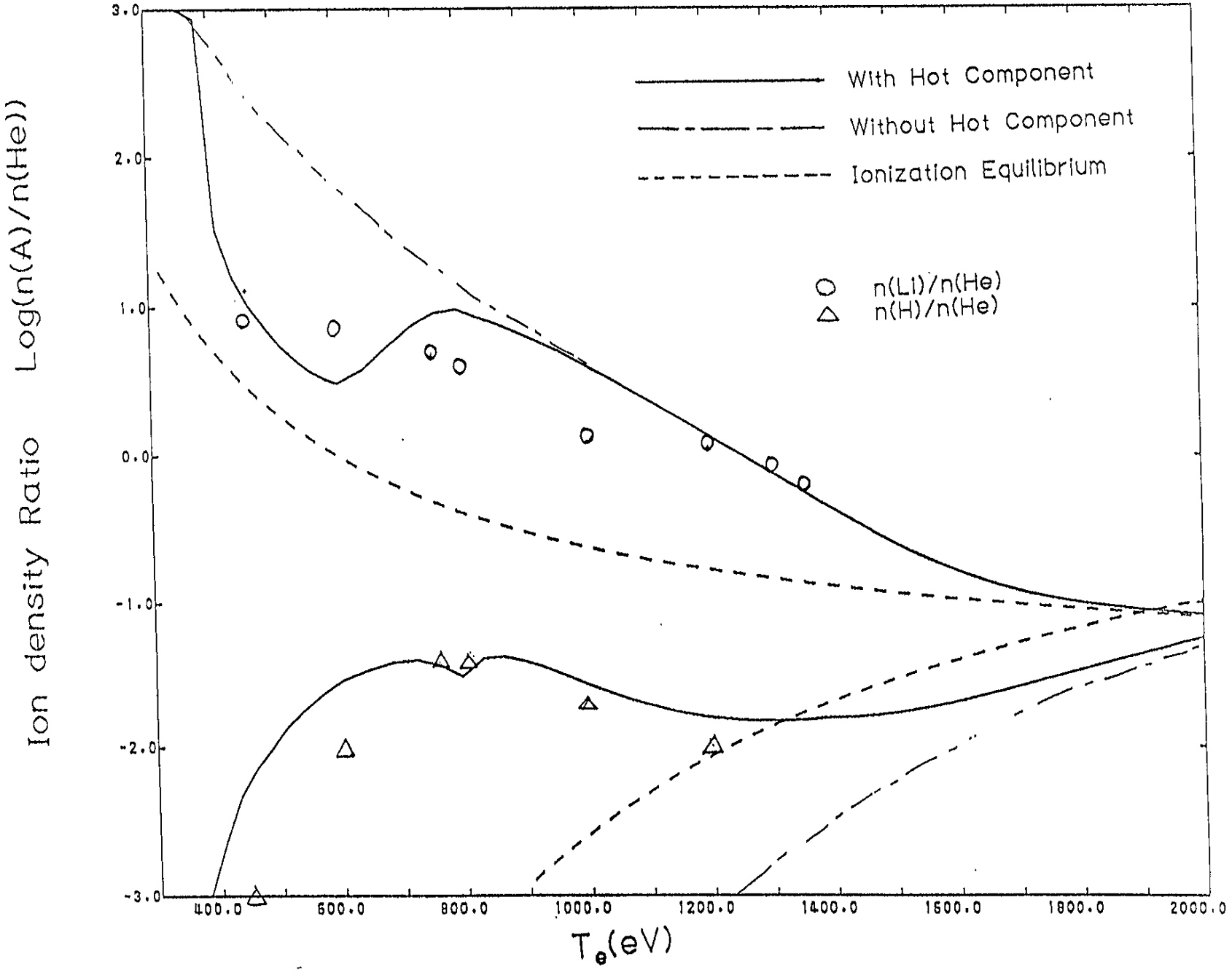
With Hot Component
Without Hot Component
Ionization Equilibrium
n(LI)/n(He)
n(H)/n(He)
Ion density Ratio Log(n(A)/n(He))
3.0
2.0
1.0
0.0
-1.0
-2.0
-3.0
400.0
600.0
800.0
1000.0
1200.0
1400.0
1600.0
1800.0
2000.0
T_e(eV)

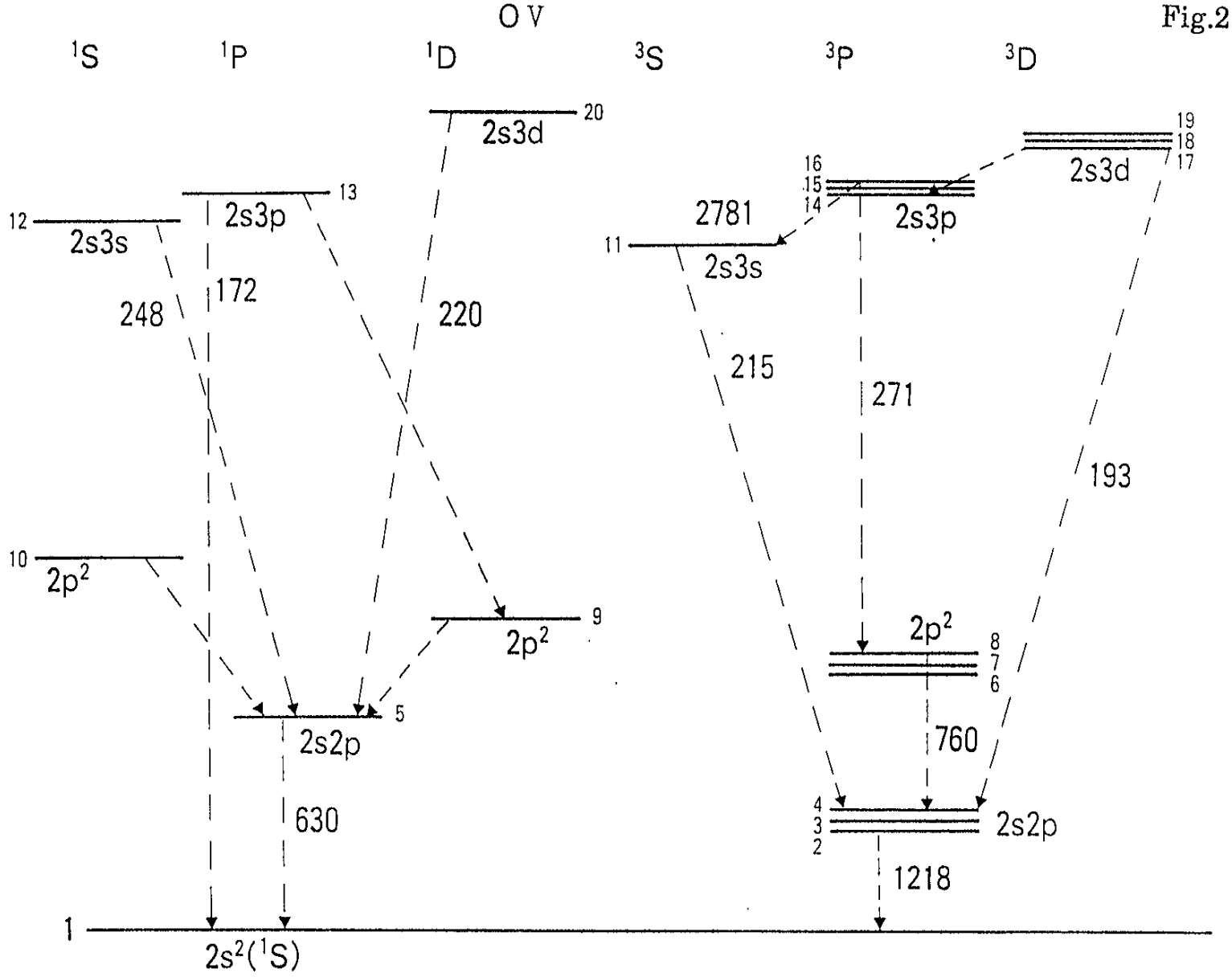
O V
1S
1P
1D
3S
3P
3D
20
2s3d
13
2s3p
12
2s3s
248
172
220
10
2p2
9
2p2
5
2s2p
630
1
2s2(1S)
19
18
17
2s3d
16
15
14
2s3p
2781
11
2s3s
215
271
193
2p2
8
7
6
760
4
3
2
2s2p
1218

Fig.2.1.

Fig.2.2.

I(172) / I(630)

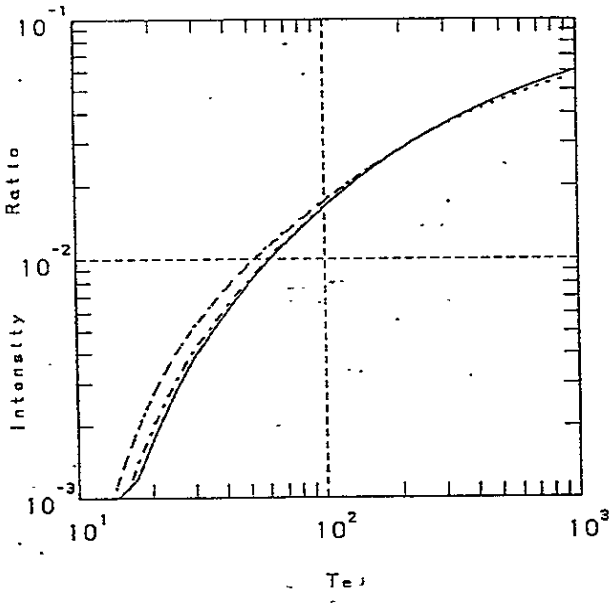

Fig.2.3.(a)

I(220) / I(172)

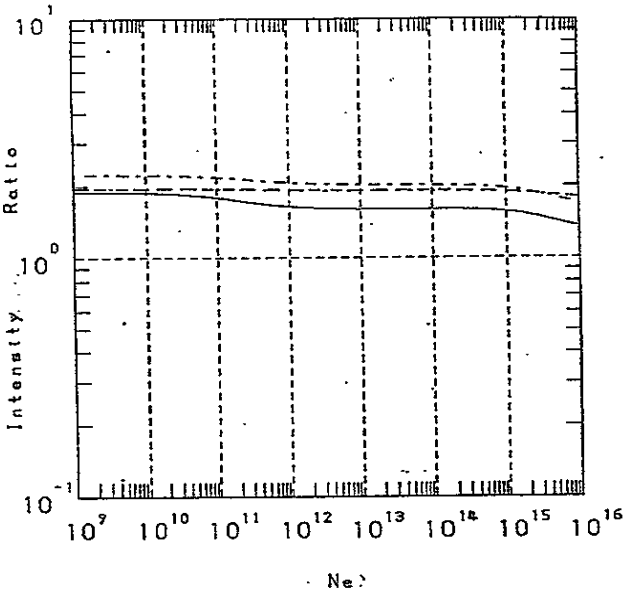

Fig.2.3.(b)

I(760) / I(630)
I(1218) / I(630)

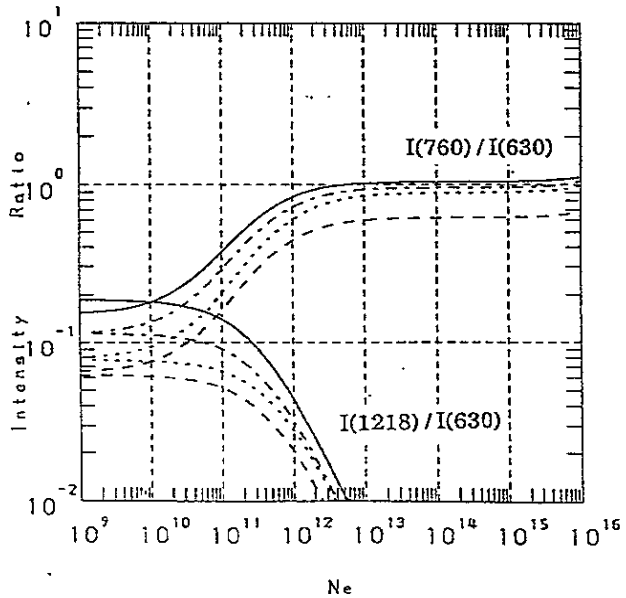

Fig.2.4.

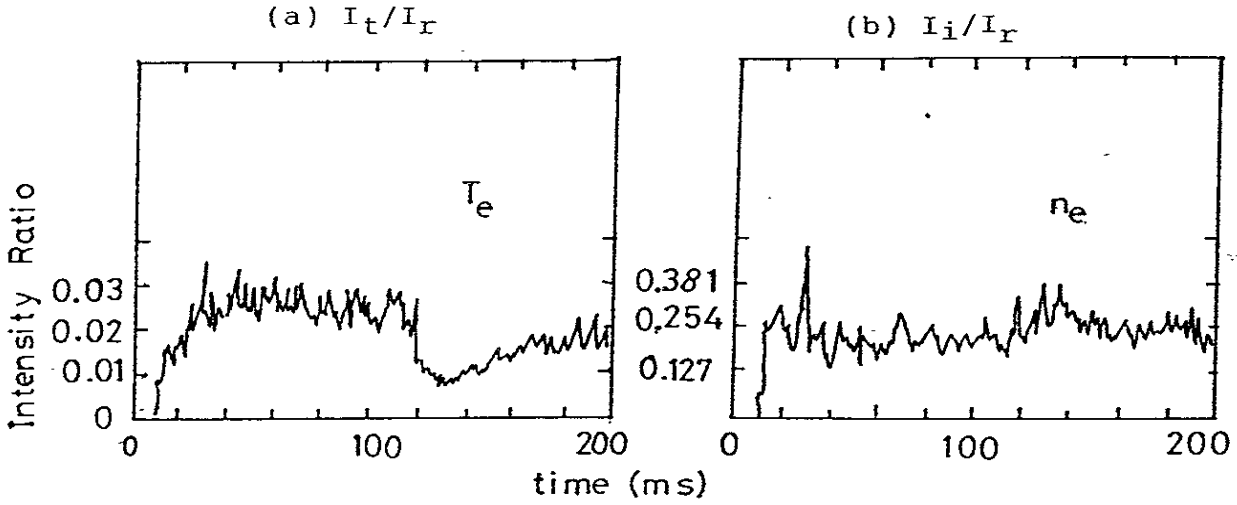
(a) I_t/I_r
(b) I_i/I_r
T_e
n_e
Intensity Ratio
0.03
0.02
0.01
0
0.381
0.254
0.127
0
100
200
0
100
200
time (ms)

Fig.2.5.

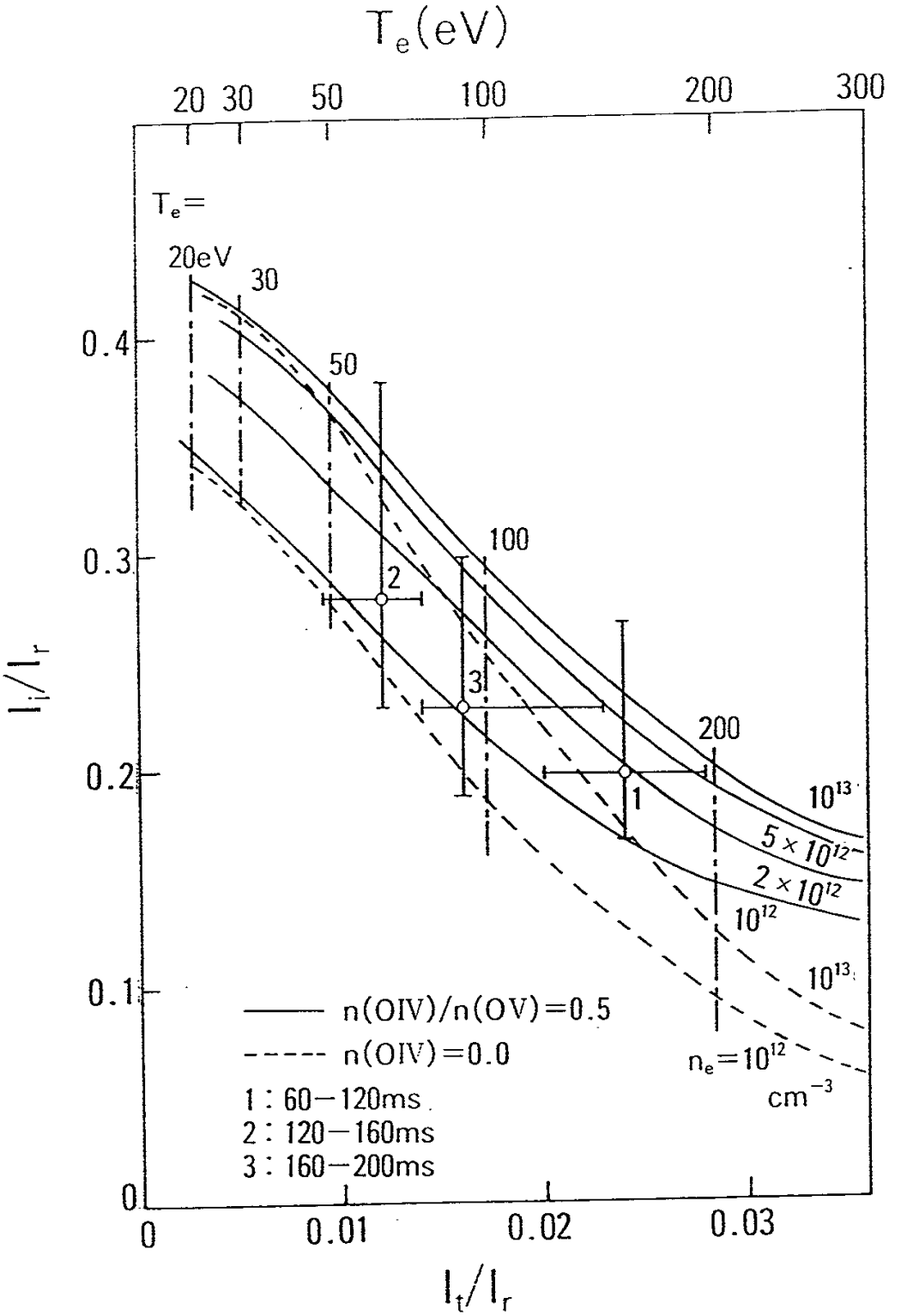
T_e(eV)
20 30 50 100 200 300
T_e=
20eV
30
50
100
200
0.4
0.3
0.2
0.1
0
I_i/I_r
2
3
1
10^{13}
5×10^{12}
2×10^{12}
10^{12}
10^{13}
n(OIV)/n(OV)=0.5
n(OIV)=0.0
$n_e=10^{12}$ cm^{-3}
1 : 60−120ms
2 : 120−160ms
3 : 160−200ms
0
0.01
0.02
0.03
I_t/I_r

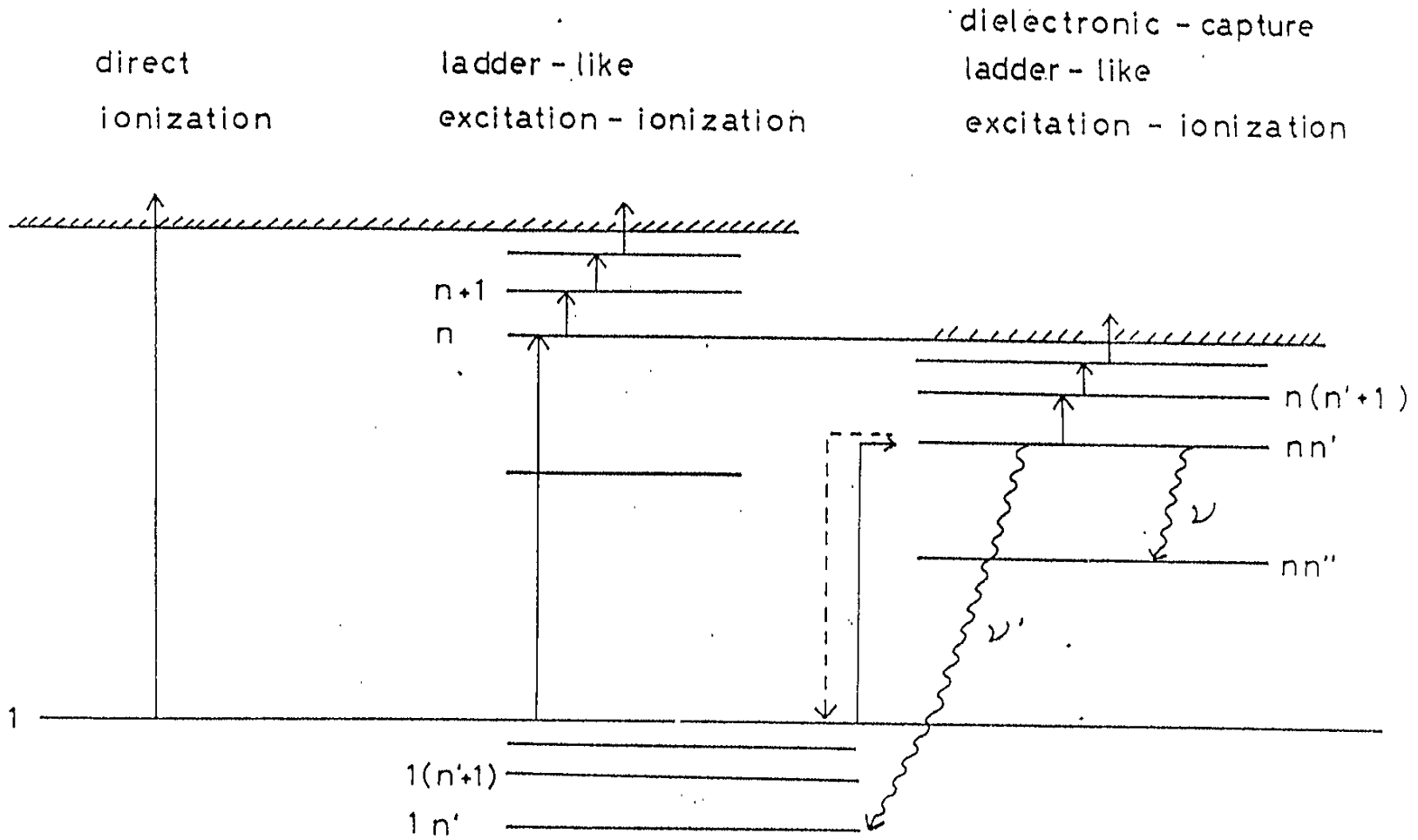
direct
ionization
ladder - like
excitation - ionization
dielectronic - capture
ladder - like
excitation - ionization
n+1
n
n(n'+1)
nn'
ν
nn''
ν'
1
1(n'+1)
1 n'

Fig.3.1.

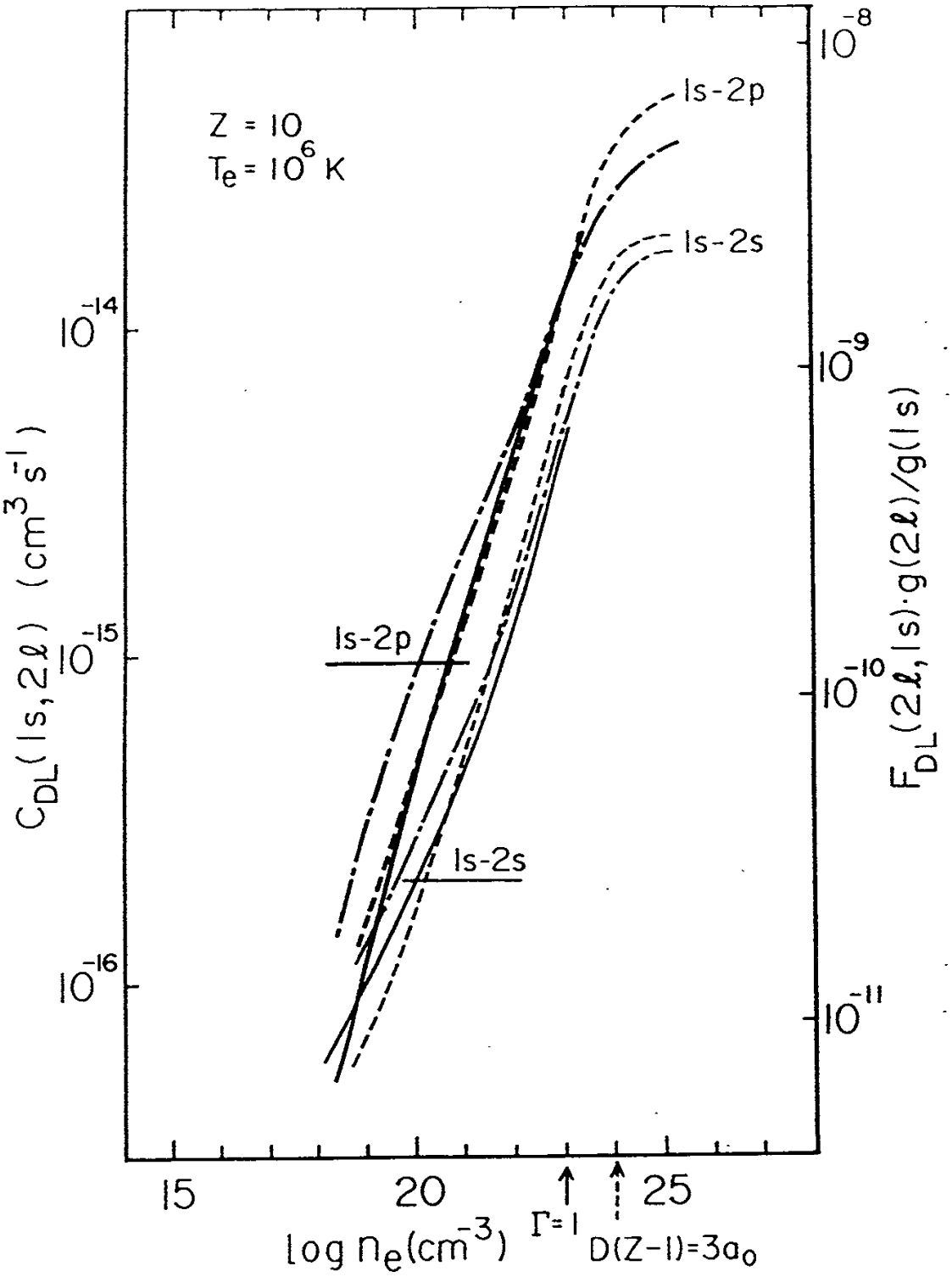
Z = 10
Te = 10^6 K
1s-2p
1s-2s
1s-2p
1s-2s
10^-14
10^-15
10^-16
10^-8
10^-9
10^-10
10^-11
C_DL(1s,2ℓ) (cm^3 s^-1)
F_DL(2ℓ,1s)·g(2ℓ)/g(1s)
15
20
25
log ne(cm^-3)
Γ=1
D(Z-1)=3a0

Fig.3.2.

Fig.3.3.

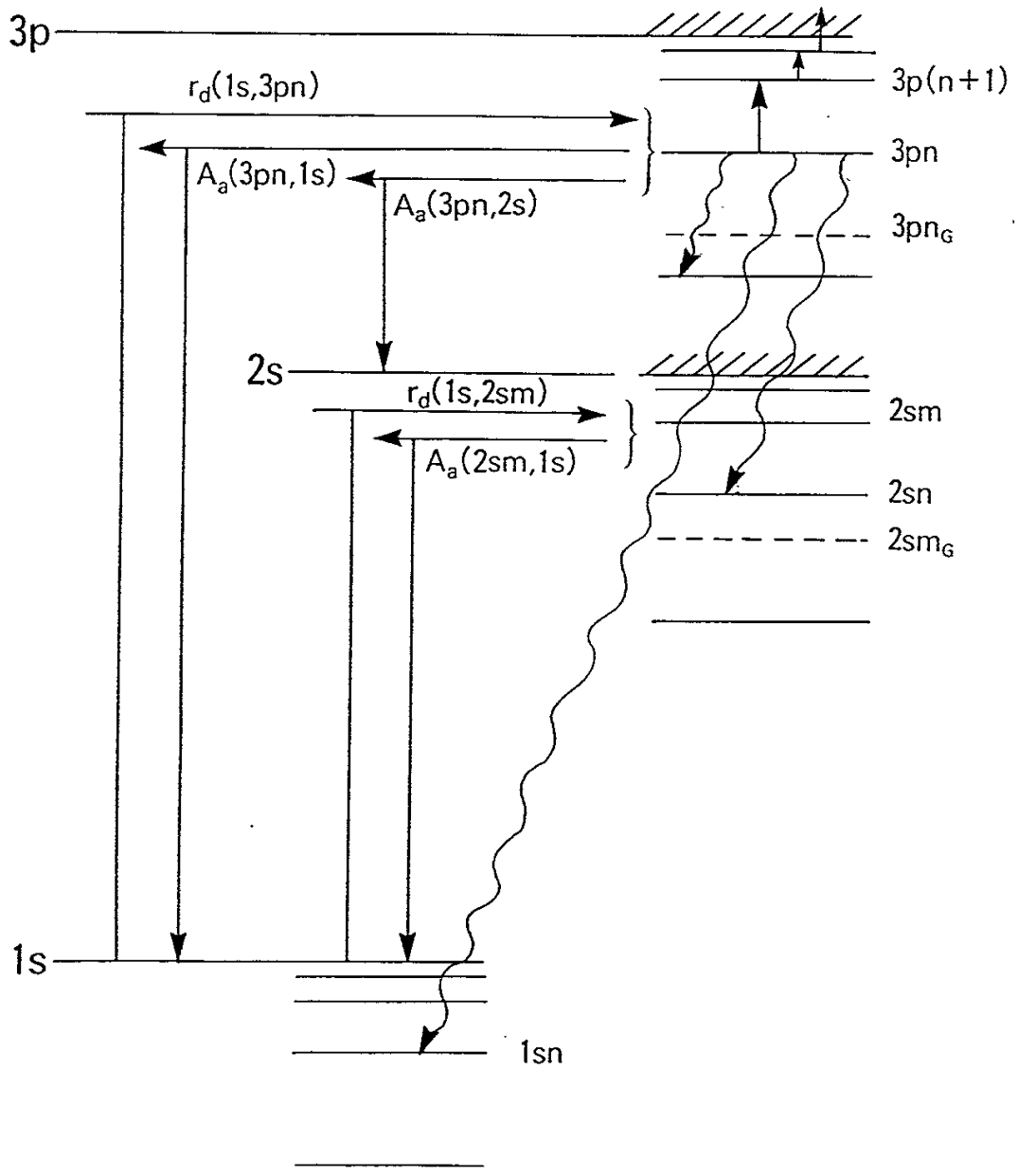
3p
r_d(1s,3pn)
A_a(3pn,1s)
A_a(3pn,2s)
2s
r_d(1s,2sm)
A_a(2sm,1s)
1s
3p(n+1)
3pn
3pn$_G$
2sm
2sn
2sm$_G$
1sn

Fig.3.4.

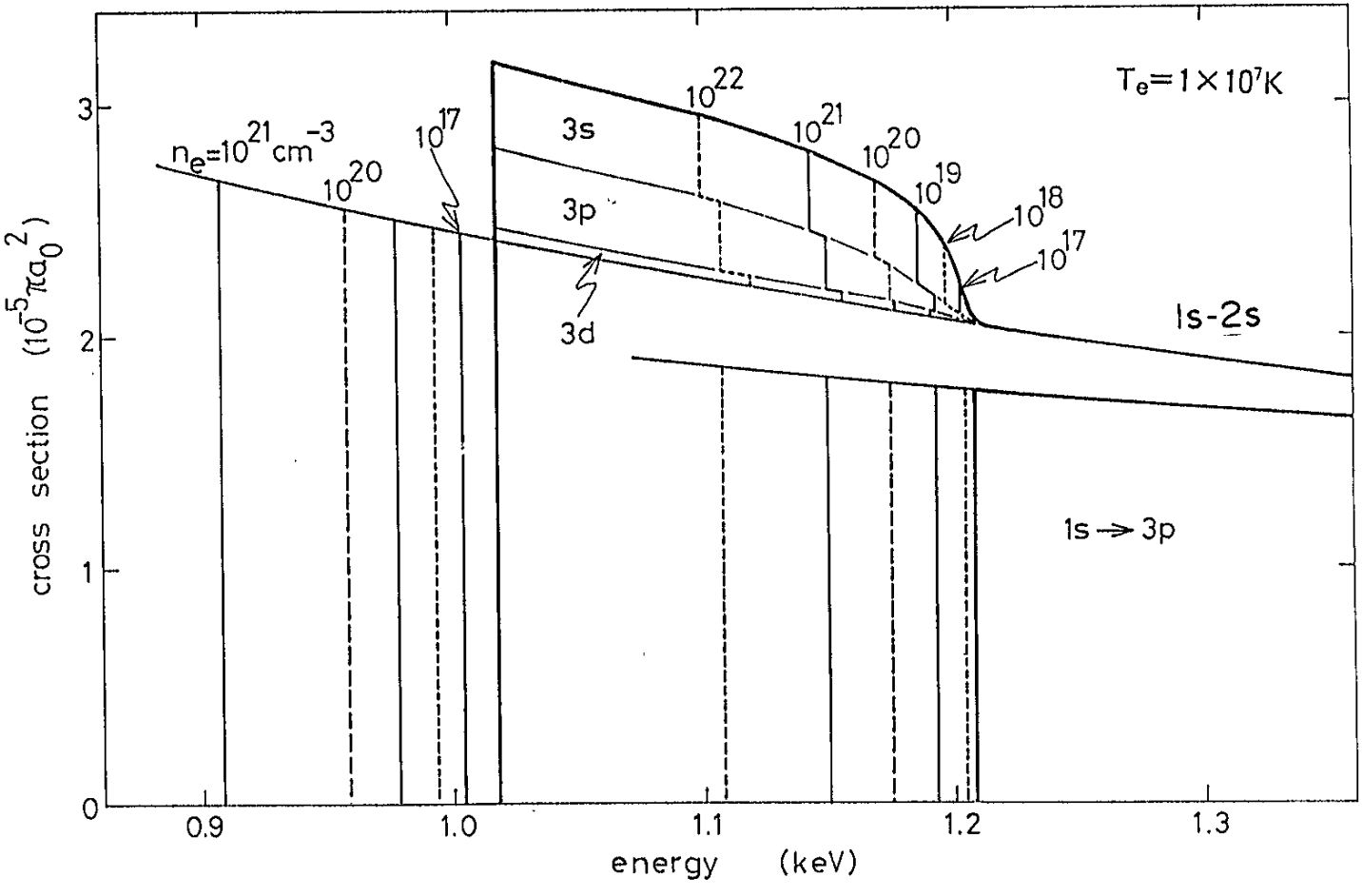
$T_e = 1 \times 10^7$K
$n_e = 10^{21}$ cm^{-3}
10^{22}
10^{21}
10^{20}
10^{19}
10^{18}
10^{17}
10^{20}
10^{17}
3s
3p
3d
1s-2s
1s → 3p
cross section ($10^{-5}\pi a_0^2$)
energy (keV)
0
1
2
3
0.9
1.0
1.1
1.2
1.3

Fig.3.5.

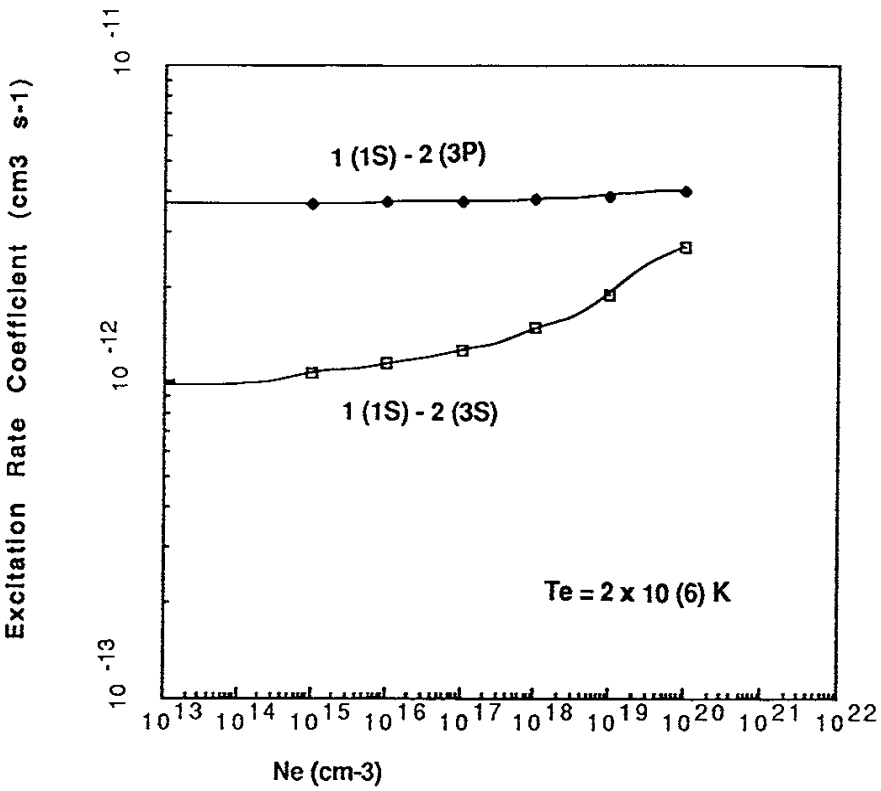
Excitation Rate Coefficient (cm3 s-1)
10 -11
10 -12
10 -13
1 (1S) - 2 (3P)
1 (1S) - 2 (3S)
Te = 2 x 10 (6) K
10^13 10^14 10^15 10^16 10^17 10^18 10^19 10^20 10^21 10^22
Ne (cm-3)